Double Heterohelicenes Composed of Benzo[*b*]- and Dibenzo[*b*,*i*]phenoxazine: A Comprehensive Comparison of Their Electronic and Chiroptical Properties

Daisuke Sakamaki, Shunya Tanaka, Katsuki Tanaka, Mayu Takino, Masayuki Gon, Kazuo Tanaka, Takashi Hirose, Daichi Hirobe, Hiroshi M. Yamamoto, and Hideki Fujiwara**

Dr. D. Sakamaki, S. Tanaka, K. Tanaka, M. Takino, Prof. Dr. H. Fujiwara

Department of Chemistry, Graduate School of Science, Osaka Prefecture University, Naka-ku, Sakai-shi, Osaka 599-8531 (Japan)

E-mail: sakamaki@c.s.osakafu-u.ac.jp

hfuji@c.s.osakafu-u.ac.jp

Dr. M. Gon, Prof. Dr. K. Tanaka

Department of Polymer Chemistry, Graduate School of Engineering, Kyoto University, Nishikyo-ku, Kyoto 615-8510 (Japan)

Prof. Dr. T. Hirose

Institute for Chemical Research, Kyoto University, Uji, Kyoto 611-0011 (Japan)

PRESTO, Japan Science and Technology Agency (JST), Kawaguchi, Saitama 332-0012 (Japan)

Dr. D. Hirobe

Institute for Molecular Science, Myodaiji, Okazaki, 444-8585 (Japan)

SOKENDAI (Graduate University for Advanced Studies), Myodaiji, Okazaki 444-8585 (Japan)

PRESTO, Japan Science and Technology Agency (JST), Kawaguchi, Saitama 332-0012 (Japan)

Prof. Dr. H. M. Yamamoto

Institute for Molecular Science, Myodaiji, Okazaki, 444-8585 (Japan)

SOKENDAI (Graduate University for Advanced Studies), Myodaiji, Okazaki 444-8585 (Japan)

‡Supporting information for this article is available on the WWW under http:xxxx

Keywords: azaacene • oxidative coupling • helicene • circularly polarized luminescence • organic field effect transistor

ABSTRACT

Heterohelicenes are potential materials in molecular electronics and optics because of their inherent chirality and various electronic properties originating from the introduced heteroatoms. In this work, we comprehensively investigated two kinds of double NO-hetero[5]helicenes composed of 12*H*-benzo[*b*]phenoxazine (**BPO**) and 13*H*-dibenzo[*b*,*i*]phenoxazine (**DBPO**). These helicenes exhibit good electron donor property reflecting the electron-rich character of their monomers and were demonstrated to work as p-type semiconductors. The enantiomers of these helicenes show the largest class of dissymmetry factors for circularly polarized luminescence (CPL) ($|g_{CPL}| > 10^{-2}$) among the previously reported helicenes. Interestingly, the signs of CPL are opposite between **BPO**- and **DBPO**-double helicenes of the same helicity. The origin of the large g_{CPL} values and the inversion of the CPL signs was addressed by analysis of the transition electronic dipole moments (TEDM) and transition magnetic dipole moments (TMDM) based on the TD-DFT calculations.

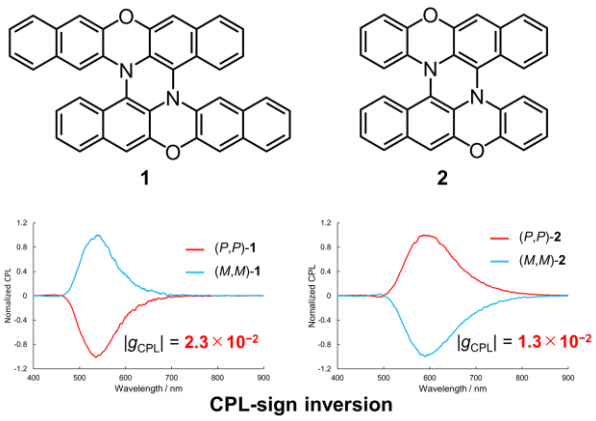

π-Conjugated molecules with inherent chirality have received increasing attention in recent years due to their optical and electronic properties, such as circular dichroism (CD), circularly polarized luminescence (CPL),[1] and chirality-induced spin selectivity (CISS).[2] Helicenes, which are ortho-fused polycyclic aromatic hydrocarbons, are an outstanding class of chiral π-conjugated molecules.[3–6] In particular, multiple helicenes, where more than one helicene moieties exist in a single molecule,[7] have attracted intense recent interest as potential materials with strong chiroptical properties.[8–11] Over the past two decades, a growing number of multiple heterohelicenes have been developed using various synthetic strategies.[12–24] In 2015, we reported a facile approach for double hetero[5]helicenes by tandem oxidative coupling of heteroacenes with a NH group,[16,17] such as *N*,*N'*-dihydrodiazaacenes[25,26] and a phenothiazine.[27] The double heterohelicenes obtained by this strategy exhibit multiple oxidation processes reflecting the electron donor property of their monomers. A double NO-hetero[5]helicene **1** (Figure 1) is an example of such double heterohelicenes synthesized by oxidative coupling of two 13*H*-dibenzo[*b*,*i*]phenoxazines (**DBPO**).[16] In this work, we synthesized a novel double NO-hetero[5]helicene composed of two 12*H*-benzo[*b*]phenoxazines (**BPO**) (**2** in Figure 1), and we comprehensively compared the structures and the physical properties of **1** and **2**, including their chiroptical properties (CD and CPL) and field effect transistor (FET)

properties. As a result, we found that **1** and **2** are CPL emitters with the largest class of the dissymmetry factor of CPL (g_{CPL}) among (hetero)helicenes reported so far. The origin of the large g_{CPL} values of **1** and **2** was theoretically investigated based on the analysis of their transition electronic dipole moments (TEDM) and transition magnetic dipole moments (TMDM).

As reported in our previous work, the oxidation of **DBPO** with DDQ selectively gave a cruciform dimer with a C–N bond between the nitrogen atom of one **DBPO** and an *ortho*-carbon to the nitrogen atom (C12) of the other **DBPO**. In contrast to **DBPO**, **BPO** is asymmetric in the longitudinal direction and has an unsubstituted *para*-carbon atom to the nitrogen atom (C3), so the oxidative dimerization of **BPO** may give some structural isomers. However, the oxidation of **BPO** with 0.5 eq. of DDQ selectively gave a cruciform dimer **3** connected with a C11–N bond in 79% yield. This result was similar to the oxidative dimerization of mono *N*-alkylated 5,12-dihydro-5,12-diazatetracene.[28] In 1969, VanAllan reported that the oxidation of **BPO** with various oxidants (cupric acetate, hydrogen peroxide, benzoquinone, cobalt acetate, and potassium permanganate) gave a dimer of **BPO**, and they assigned it to **3**, but the structure of the dimer was not determined experimentally at that time.[29] Because we could not obtain good single crystals of **3** due to the low solubility, we synthesized the *N*-propylated derivative (**3$_{Pr}$**) and succeeded in

determining the connectivity of the dimer by the X-ray single crystal analysis (Figure S5). The cruciform dimer **3** was successfully converted to a double *N*-hetero[5]helicene **2** in 69% yield by the ring-fusion reaction with DDQ and $Sc(OTf)_3$. **2** was also obtained from **BPO** in a one-pot manner without isolating **3** in a moderate yield (42%), and this yield was also higher than that of **1** by the one-pot reaction from **DBPO** (10%). The much-improved yield of **2** compared to **1** could be attributed to the absence of the dimerization of **3**, whereas the tetramer of **DBPO** with a hash-mark-shaped structure[30] was competitively formed in the ring-fusion to **1**. **1** and **2** are well soluble in common organic solvents, such as toluene, dichloromethane, chloroform, and THF (e.g. > 20 mg / mL in dichloromethane), despite the absence of substituents.

The single crystals of racemic-**2** were obtained by slow diffusion of methanol into a toluene solution of **2**, and X-ray analysis successfully revealed the crystal structure. The space group of the crystal is $P\bar{1}$. There are two crystallographically independent molecules in a unit cell, but their structures are almost the same. Figure 2a shows the structure of one (*M*,*M*)-enantiomer of **2** in the racemic crystal. The average torsion angle around helicene moieties of **2** was 48.3(3)°, and this value was close to that of **1** (45.8(2)°).[16] The bond lengths of **2** were also close to those of **1** (Figure S6). Despite the structural similarity of **1** and **2**, their packing structures were completely different. In the

crystal of racemic-**2**, each enantiomer was aligned in columnar stacks along the *b*-axis (Figure 2b). This packing structure is in contrast to that of **1**, where opposite enantiomers are stacked alternatively (Figure S7). In the homochiral columns of **2** in the racemic crystal, some short intermolecular contacts were observed due to π/π and CH/π interactions, and the shortest intermolecular C---C distance was 3.25 Å. In addition to the intracolumnar interactions, intercolumnar π/π, and CH/π interactions were also observed, and the shortest C---C contact between opposite enantiomers was 3.31 Å.

DFT optimization of **2** at the B3LYP-GD3BJ/6-311G(2d,p) level of theory gave the C_2 symmetric structure, similar to the case of **1**. As shown in Figure 3, the frontier Kohn-Sham MOs of **1** and **2** are equally delocalized over the two monomer units. The calculated HOMO level of **2** (−4.80 eV) is higher than that of **BPO** (−5.06 eV) by 0.26 eV and even higher than that of **1** (−4.89 eV) by 0.09 eV, indicating the increased electron donor property of **2**. In actuality, **2** showed two couples of reversible one-electron oxidation waves similar to **1** in the cyclic voltammogram, and the first oxidation potential of **2** was negatively shifted by 0.10 V compared to **1** (Figure S11 and Table S5). Both in **1** and **2**, HOMO and LUMO belong to irreducible representation (irrep) *a*. The TD-DFT calculated oscillator strengths for the $S_0 \rightarrow S_1$ transitions (HOMO (*a*)→LUMO (*a*): 100%) of **1** and **2** were very small (0.0018 for **1** and 0.0002 for **2**) because the electronic

transitions perpendicular to the C_2 axis are symmetry forbidden. The transitions between MOs with different irrep, such as HOMO (*a*)→LUMO+1 (*b*) or HOMO−1 (*b*)→LUMO (*a*), had larger oscillator strengths.

The unique molecular packings and electron-rich character of racemic **1** and **2** encouraged us to investigate the semiconductive properties by using their field-effect transistors with gold electrodes. The drain-voltage (V_d) dependences of drain currents (I_d) are shown in Figure 4 for several gate voltages (V_g). Both **1** and **2** conduct discernible I_d only when negative V_g is applied, which means that **1** and **2** work as p-type transistors. This can be attributed to the shallow HOMO energy levels of **1** (−4.89 eV) and **2** (−4.80 eV). Since the values of these HOMO energy levels are very close to the high work function of gold electrodes processed in air (~ −4.7 eV),[31] this matching facilitates hole injection from the electrodes. By contrast, the values of the LUMO energy levels of **1** (−1.72 eV) and **2** (−1.62 eV) severely mismatches the work function of gold electrodes by ~3 eV, which suppresses electron injection from the gold electrodes. Although the hole mobilities of **1** and **2** were not so high (~2×10^{-5} cm^2 V^{-1} s^{-1}) and smaller than those reported for other double helicenes,[18,32] the semiconductive properties of **1** and **2** indicate potential applications in organic optoelectronic materials.

Figure 5a shows the electronic absorption spectra of racemic-**1** and **2** in

dichloromethane. **2** showed strong absorption bands ($\varepsilon > 10^4$ M^{-1} cm^{-1}) covering the range of 250–400 nm, and these bands were slightly blue-shifted compared with the corresponding peaks of **1**. Similar to the cases of **1**, **2** showed a weak absorption band around 450 nm, which is attributable to the almost forbidden HOMO→LUMO transition (Figure 3). Figure 5b shows the emission spectra of racemic-**1** and **2** in dichloromethane. The emission quantum efficiencies of **1** and **2** were decreased to about 4% compared with their monomers (**DBPO**: 26% and **BPO**: 22%), reflecting the almost forbidden HOMO-LUMO transitions of **1** and **2**. The emission peak of **2** (587 nm) was slightly red-shifted than **1** (569 nm) by 539 cm^{-1}, whereas the lowest absorption bands were almost identical for **1** and **2**. This trend was consistent with the results of TD-DFT calculations (Table S6). The emission spectra of **1** and **2** showed almost no solvent dependence in dichloromethane, acetone, and toluene (Figure S12). The fluorescence lifetimes of **1** and **2** in dichloromethane were 13.4 and 21.1 ns, respectively, and these values were an order of magnitude longer than those of **DBPO** (2.58 ns) and **BPO** (2.59 ns) (Figure S13).

The (*P*,*P*)- and (*M*,*M*)-enantiomers of **2** were easily separated using an HPLC with a chiral silica gel column under the same conditions as used for the resolution of **1** (Figure S10). Furthermore, the optical resolution of **1** and **2** was also succeeded using a chiral column for medium pressure liquid chromatography (MPLC), which can separate

a larger amount of racemic mixture at a time. By using the chiral MPLC column, 25 mg of each enantiomer was isolated within an hour. We could obtain single crystals of enantiopure **2**, whereas enantiopure **1** did not give good crystals for X-ray analysis. Judging from the X-ray crystal analysis (Figure S8 and S9) and the experimental and theoretical CD spectra (Figure S15), the faster eluting enantiomer from the chiral column is (*P*,*P*)-**2**, as is the case for **1** assigned by comparing the experimental and theoretical CD spectra. No racemization of enantiopure **2** was observed after heating in toluene at 100 ℃ for 13 hours, similar to **1**.

We compared the chiroptical properties of **1** and **2**. The CD spectra of (*P*,*P*)- and (*M*,*M*)-**2** in dichloromethane were mirror images of each other (Figure 6a and 6b). Similar to the cases of **1** and the double hetero[4]helicene composed of two phenothiazines,[16,17] (*M*,*M*)-**2** showed the first positive Cotton effect, and the sign and the shape of the observed CD spectra were well-simulated by TD-DFT calculations (Figure S14 and S15). The experimental g_{CD} values of (*M*,*M*)-**1** and **2** (at 470 nm) were $+1.7 \times 10^{-2}$ and $+1.3 \times 10^{-2}$, respectively.

The CPL spectra of **1** have not been measured in our previous work,[16] and here we carried out a comparative investigation of the CPL properties of **1** and **2**. Both of **1** and **2** in dichloromethane exhibited distinct CPL emission as shown in Figure 6c and 6d.

For the enantiomers of **1**, the signs of CPL and the lowest-energy CD were consistent. On the other hand, interestingly, the signs of CPL and that of the lowest-energy CD band were inverted for **2**; (*M*,*M*)-**2** showed the first positive CD signal and a negative CPL, and consequently (*M*,*M*)-**1** and (*M*,*M*)-**2** showed the opposite signs of CPL each other. The experimental g_{CPL} values were $+2.3 \times 10^{-2}$ (at 490 nm) for (*M*,*M*)-**1** and -1.3×10^{-2} (at 590 nm) for (*M*,*M*)-**2** (Figure S16), and **1** and **2** were found to be rare examples of CPL emitters with $|g_{CPL}|$ larger than 10^{-2} as small π-conjugated molecules.[15,33–39] The experimental values of the photophysical properties of **1** and **2** are summarized in Table 1.

To gain deeper insight into the chiroptical properties of **1** and **2**, we carefully analyzed the results of TD-DFT calculations. According to the theory,[40] the dissymmetry factor for CD (g_{CD}) is described as follows

$$g_{CD} = \frac{4|\boldsymbol{\mu}||\boldsymbol{m}| \cos \theta_{\mu,m}}{|\boldsymbol{\mu}|^2 + |\boldsymbol{m}|^2} \quad (1)$$

where $\boldsymbol{\mu}$ and $\boldsymbol{m}$ are the transition electronic dipole moment (TEDM) and transition magnetic dipole moment (TMDM) for excitation transitions, respectively, and $\theta_{\mu,m}$ is the angle between the $\boldsymbol{\mu}$ and $\boldsymbol{m}$ vectors. The dissymmetry factor for CPL (g_{CPL}) is described using $\boldsymbol{\mu}'$ and $\boldsymbol{m}'$ (TEDM and TMDM for de-excitation transitions) and $\theta_{\mu',m'}$ (the angle between $\boldsymbol{\mu}'$ and $\boldsymbol{m}'$ vectors) in a similar way:

$$g_{\mathrm{CPL}} = \frac{4|\boldsymbol{\mu}'||\boldsymbol{m}'|\cos\theta_{\mu',m'}}{|\boldsymbol{\mu}'|^2 + |\boldsymbol{m}'|^2} \quad (2).$$

Eqs. 1 and 2 indicate that the absolute values of g_{CD} and g_{CPL} are maximized under the following conditions: (i) the magnitude of the TEDM and TMDM vectors are the same and (ii) the directions of the TEDM and TMDM vectors are parallel or antiparallel. We analyzed the TEDM and TMDM of **1** and **2** at the optimized geometries in the S_0 and S_1 states and calculated the dissymmetry factors for CD and CPL. In addition, we performed density mapping of TEDM and TMDM to visualize the origin of the magnitudes of TEDM and TMDM.[38,39] The total TEDM and TMDM densities ($\rho^{\mu}_{\mathrm{total}}$ and $\rho^{m}_{\mathrm{total}}$) are expressed as the density forms of TEDM and TMDM, whose space integrals give the magnitudes of TEDM and TMDM.[39] As a reference molecule, we analyzed a double carbohelicene **4**, which is an all-carbon analogue of **2**, to investigate the effect of heteroatom substitution. Structural optimization predicted that all of **1**, **2**, and **4** have the C_2 symmetric structures both in the S_0 and S_1 states. Figure 7 summarizes the results of TEDM and TMDM analysis for the (*M*,*M*)-isomers. TD-DFT calculations correctly reproduced the experimental signs of g_{CD} and g_{CPL} of **1** and **2**, including the inversion of the signs of CD and CPL observed in **2** (Table S6 and S7). The opposite sign of CD and CPL of **2** was predicted to originate from the inversion of the directions of TEDM between the S_0 and S_1 states (Table S8). Both **1** and **2** were predicted to have huge dissymmetry

factors ($|g_{CD}|$ = 0.11, $|g_{CPL}|$ = 0.31 for **1** and $|g_{CD}|$ = 0.34, $|g_{CPL}|$ = 1.19 for **2**, Figure 7 and Table S6). One reason for the large dissymmetry factors of **1** and **2** is the ideal angles between the TEDM and TMDM vectors (0° or 180°), and another is the well-balanced magnitudes of the TEDM and TMDM. In C_2 symmetric molecules, both TEDM and TMDM become parallel to the C_2 axis (set as the *z*-axis) on the transitions between MOs with the same irrep. Because $S_0 \rightarrow S_1$ and $S_1 \rightarrow S_0$ transitions of **1** and **2** are pure HOMO (irrep. *a*)–LUMO (irrep. *a*) transitions, the ideal angle between the TEDM and TMDM vectors (0° or 180°) is realized ($\cos\theta_{\mu,m} = \cos\theta_{\mu',m'} = 1$ for (*M*,*M*)-**1** and $\cos\theta_{\mu,m} = 1$, $\cos\theta_{\mu',m'} = -1$ for (*M*,*M*)-**2**, Figure S23, S24, 8a, and 9a). The reason for the well-balanced magnitude of the TEDM and TMDM of **1** and **2** is the reduced TEDM magnitudes and the moderately large TMDM magnitudes. In general, the magnitude of TEDM is much larger than that of TMDM in most organic molecules, and the mismatch of these magnitudes results in the small dissymmetry factors. For **1** and **2**, only the *z* component of the TEDM vector has a non-zero value for the HOMO–LUMO transition due to the symmetry constraint. Because the *z*-axis is almost perpendicular to the π-planes of quasi-planar **1** and **2**, the magnitude of the TEDM vectors becomes inevitably small for these transitions (17.9×10^{-20} esu·cm for **1** and 4.5×10^{-20} esu·cm for **2**, in the S_1 states) (Figure 7b and Table S6). On the other hand, the magnitudes of TMDM of **1** and **2** were relatively

large for small π-conjugated molecules (1.38×10^{-20} erg·G^{-1} for **1** and 1.49×10^{-20} erg·G^{-1} for **2**, in the S_1 states) (Figure 7b and Table S6). The density mapping visually explains the small TEDM and the large TMDM of **1** and **2**. In the TEDM densities ($\rho^{\mu}_{\mathrm{total}}$) of **1**, the blue (positive) region is slightly larger than the red (negative) region both for the $S_0 \rightarrow S_1$ and $S_1 \rightarrow S_0$ transitions. This means that most TEDM densities cancel each other out, and the directions of the TEDM are the same in the $S_0 \rightarrow S_1$ and $S_1 \rightarrow S_0$ transitions. In the $S_0 \rightarrow S_1$ transition of **2**, the blue area is also slightly larger than the red area, suggesting a positive TEDM along the z-axis. On the other hand, in the $S_1 \rightarrow S_0$ transition of **2**, the red region became slightly larger than the blue region, leading to the inversion of the direction of TEDM. Both in the TMDM densities ($\rho^{m}_{\mathrm{total}}$) of (*M*,*M*)-**1** and **2**, red region is dominant, resulting in larger magnitudes of TMDM. The TMDM densities of **1** and **2** are mainly distributed on their central six-membered ring with two nitrogen atoms and the outer regions of the naphthalene moieties fused to the central ring. In contrast to **1** and **2**, double carbohelicene **4** was predicted to have much larger magnitudes of TEDM (619×10^{-20} esu·cm in the S_1 states) and much smaller magnitudes of TMDM (0.03×10^{-20} erg·G^{-1} in the S_1 states) (Figure 7b). The reason for the larger TEDM is that HOMO and LUMO of **4** belong to irrep *a* and irrep *b*, respectively (Figure S27). The TMDM densities of **4** are almost completely vanished, leading to very small magnitudes of TMDM. Due

to the mismatch between the magnitudes of TEDM and TMDM, the dissymmetry factors of **4** were drastically reduced less than a few tenths of **1** and **2** ($|g_{CD}| = 2.6 \times 10^{-4}$ and $|g_{CPL}| = 1.9 \times 10^{-4}$ for **4**).

As described above, theoretical calculations predicted that **1** and **2** exhibit huge $|g_{CPL}|$ values (0.31 for **1** and 1.19 for **2**) due to the well-balanced ratios and the ideal orientation of TEDM to TMDM, but these values were overestimated compared to the experimental ones (0.023 for **1** and 0.013 for **2**). In addition, the theoretical fluorescence emission rate constants (k_f) calculated at the C_2 symmetric S_1 states (5.0×10^4 s^{-1} for **1** and 1.1×10^3 s^{-1} for **2**, Table S9 and S11) were too small compared to the experimental values (2.8×10^6 s^{-1} for **1** and 1.7×10^6 s^{-1} for and **2**, Table 1). The discrepancies between theory and experiment probably arise because only the Frank-Condon (FC) transitions at the perfect C_2 symmetric structures were assumed in the TD-DFT calculations. Symmetry forbidden transitions can become partially allowed by vibronic coupling with symmetry-lowering vibrational modes.[41–43] To examine how structural deformation affects $|g_{CPL}|$ and k_f, we performed single point TD-DFT calculations for the S_1 states of **1** and **2** by gradually varying their geometries along the selected low-frequency modes. For simplicity, here we only consider the symmetrical (irrep *a*) and asymmetrical (irrep *b*) stretching modes of two helical pitches. The lowest-frequency mode of **1** (mode 1, 20.0

cm^{-1}, Figure S18) and the lowest- and second-lowest frequency modes of **2** (mode 1, 38.2 cm^{-1}, and mode 2, 42.4 cm^{-1}, Figure S20 and S21) were the symmetrical stretching modes of two helical pitches. The asymmetrical stretching of two helical pitches was the third-lowest mode for **1** (mode 3, 39.3 cm^{-1}, Figure S19) and the fourth-lowest mode for **2** (mode 4, 69.3 cm^{-1}, Figure S22). Figure 8 and 9 show how the TEDM (***μ***') and TMDM (***m***') vectors of **1** and **2** change by the asymmetrical deformation. As the asymmetrical deformation of two helical pitches proceeds, the TEDM vector gradually tilts from the *z* axis, and simultaneously, the magnitude of TEDM increases. On the other hand, the magnitude and direction of TMDM are almost unchanged by the asymmetrical deformation. Consequently, it is theoretically estimated that $|g_{CPL}|$ decreases drastically and k_f increases by the asymmetrical deformation (Table S10 and S13). For example, $|g_{CPL}|$ of **2** decreases to 0.041 and k_f increases to 9.9×10^4 s^{-1} at the asymmetric structure whose helical pitches asymmetrically changed to 32.2° and 44.2° from 38.2° in the equilibrium state (Figure 9c and Table S13). This structure is only 7.8 kJ mol^{-1} higher in energy than the most stable C_2 structure, suggesting that the slight asymmetric deformation can drastically affect the chiroptical properties of **1** and **2**. On the other hand, the ***μ***' and ***m***' vectors remained parallel or antiparallel upon the symmetrical deformation of two helical pitches (Table S9, S11, and S12) both in **1** and **2**. For **1**, the values of g_{CPL}

and k_f are almost unchanged upon the deformation along mode 1 (Table S9). For **2**, mode 1 and mode 2 shift the values of g_{CPL} in the opposite way, and therefore the amount of change of g_{CPL} will be somewhat cancelled out. Furthermore, these two modes do not increase k_f significantly (Table S11 and S12). Of course, this discussion is a simplified treatment of the molecular deformation, but it can qualitatively reproduce the experimental results and suggests the importance of the vibronic coupling in chiroptical properties.[44]

In conclusion, we have succeeded in the synthesis of a novel double NO hetero[5]helicene (**2**) composed of two benzo[*b*]phenoxazine (**BPO**) by tandem oxidative coupling of **BPO**. The yield of **2** was much improved compared to that of the double NO hetero[5]helicene composed of two dibenzo[*b*]phenoxazine (**DBPO**) (**1**). X-ray single crystal analysis revealed that each enantiomer of **2** was stacked into a homochiral columnar structure in the racemic crystal. Reflecting the electron-rich character and dense molecular packing, **1** and **2** were proved to work as p-type transistors. (*P*,*P*)- and (*M*,*M*)-**2** were readily separated with a HPLC or MPLC equipped with chiral silica gel column. The electronic properties, in particular, chiroptical properties of **1** and **2** were investigated in detail by both experimental and theoretical methods. **1** and **2** exhibited the large g_{CPL} values of the order of 10^{-2}. By comparing the results of TD-DFT calculations for **1** and **2**

with those for the all-carbon analogue of **2**, the insertion of N and O atoms was found to enhance the g_{CPL} values of **1** and **2** drastically. The theoretical investigation indicates that the chiroptical properties of double helicenes with symmetric structures could be largely affected by the molecular deformation to the lower symmetric structures, especially when the lowest-energy transition is nearly symmetry forbidden. This work suggests the importance of considering the dynamic nature of molecular structures on analyzing and designing molecules with chiroptical properties.

ACKNOWLEDGMENTS

This work was supported by a Grant-in-Aid for Scientific Research (17H04874, 18K05264, 19H00891, 20H02726) from the Japan Society for the Promotion of Science (JSPS), a Grant-in-Aid for Transformative Research Areas (A) "Condensed Conjugation" (JSPS KAKENHI Grant Number JP20H05866) from MEXT, Grant-in-Aid Challenging Research (Exploratory) (20K20903) from JSPS, PRESTO (JPMJPR20L9) from Japan Science and Technology Agency and Ogasawara Toshiaki Memorial Foundation. The theoretical calculations were performed using Research Center for Computational Science, Okazaki, Japan.

REFERENCES

(1) Albano, G.; Pescitelli, G.; Di Bari, L. Chiroptical Properties in Thin Films of π-Conjugated Systems. *Chem. Rev.* **2020**, *120*, 10145– 10243.

(2) Kiran, V.; Mathew, S. P.; Cohen, S. R.; Hernández Delgado, I.; Lacour, J.; Naaman, R. Helicenes - A New Class of Organic Spin Filter. *Adv. Mater.* **2016**, *28*, 1957– 1962.

(3) Shen, Y.; Chen, C.-F. Helicenes: Synthesis and Applications. *Chem. Rev*. **2012**, *112*, 1463−1535.

(4) Gingras, M. One Hundred Years of Helicene Chemistry. Part 1: Non-Stereoselective Syntheses of Carbohelicenes. *Chem. Soc. Rev*. **2013**, *42*, 968−1006.

(5) Gingras, M.; Felix, G.; Peresutti, R. One Hundred Years of Helicene Chemistry. Part 2: Stereoselective Syntheses and Chiral Separations of Carbohelicenes. *Chem. Soc. Rev*. **2013**, *42*, 1007−1050.

(6) Gingras, M. One Hundred Years of Helicene Chemistry. Part 3: Applications and Properties of Carbohelicenes. *Chem. Soc. Rev*. **2013**, *42*, 1051−1095.

(7) Li, C.; Yang, Y.; Miao, Q. Recent Progress in Chemistry of Multiple Helicenes. *Chem. - Asian J*. **2018**, *13*, 884−894.

(8) Tanaka, H.; Ikenosako, M.; Kato, Y.; Fujiki, M.; Inoue, Y.; Mori, T. Symmetry-Based Rational Design for Boosting Chiroptical Responses. *Commun. Chem*. **2018**, *1*, 38.

(9) Tanaka, H.; Inoue, Y.; Mori, T. Circularly Polarized Luminescence and Circular Dichroisms in Small Organic Molecules: Correlation between Excitation and Emission Dissymmetry Factors. *ChemPhotoChem* **2018**, *2*, 386-402.

(10) Mori, T. Chiroptical Properties of Symmetric Double, Triple, and Multiple Helicenes. *Chem. Rev*. **2021**, *121*, 2373–2412.

(11) Zhao, W.-L.; Li, M.; Lu, H.-Y.; Chen, C.-F. Advances in Helicene Derivatives with Circularly Polarized Luminescence. *Chem. Commun*. **2019**, *55*, 13793−13803.

(12) Shiraishi, K.; Rajca, A.; Pink, M.; Rajca, S. π-Conjugated Conjoined Double Helicene via a Sequence of Three Oxidative CC-and NN-Homocouplings. *J. Am. Chem. Soc*. **2005**, *127*, 9312−9313.

(13) Wang, Z.; Shi, J.; Wang, J.; Li, C.; Tian, X.; Cheng, Y.; Wang, H. Syntheses and Crystal Structures of Benzohexathia[7]helicene and Naphthalene Cored Double Helicene. *Org. Lett*. **2010**, *12*, 456−459.

(14) Hashimoto, S.; Nakatsuka, S.; Nakamura, M.; Hatakeyama, T. Construction of a Highly Distorted Benzene Ring in a Double Helicene. *Angew. Chem., Int. Ed*. **2014**, *53*, 14074−14076.

(15) Nakamura, K.; Furumi, S.; Takeuchi, M.; Shibuya, T.; Tanaka, K. Enantioselective Synthesis and Enhanced Circularly Polarized Luminescence of S-Shaped Double

Azahelicenes. *J. Am. Chem. Soc*. **2014**, *136*, 5555−5558.

(16) Sakamaki, D.; Kumano, D.; Yashima, E.; Seki, S. *Angew. Chem. Int. Ed*. **2015**, *54*, 5404−5407.

(17) Sakamaki, D.; Kumano, D.; Yashima, E.; Seki, S. A Double Hetero[4]helicene Composed of Two Phenothiazines: Synthesis, Structural Properties, and Cationic States. *Chem. Commun*. **2015**, *51*, 17237−17240.

(18) Katayama, T.; Nakatsuka, S.; Hirai, H.; Yasuda, N.; Kumar, J.; Kawai, T.; Hatakeyama, T. Two-Step Synthesis of Boron-Fused Double Helicenes. *J. Am. Chem. Soc*. **2016**, *138*, 5210−5213.

(19) Wang, X.-Y.; Wang, X.-C.; Narita, A.; Wagner, M.; Cao, X.-Y.; Feng, X.; Müllen, K. Synthesis, Structure, and Chiroptical Properties of a Double [7]Heterohelicene. *J. Am. Chem. Soc*. **2016**, *138*, 12783−12786.

(20) Richter, M.; Hahn, S.; Dmitrieva, E.; Rominger, F.; Popov, A.; Bunz, U. H. F.; Feng, X.; Berger, R. Helical Ullazine-Quinoxaline-Based Polycyclic Aromatic Hydrocarbons. *Chem. - Eur. J*. **2019**, *25*, 1345−1352.

(21) Kinoshita, S.; Yamano, R.; Shibata, Y.; Tanaka, Y.; Hanada, K.; Matsumoto, T.; Miyamoto, K.; Muranaka, A.; Uchiyama, M.; Tanaka, K. Rhodium-Catalyzed Highly Diastereo- and Enantioselective Synthesis of a Configurationally Stable S-Shaped Double

Helicene-Like Molecule. *Angew. Chem., Int. Ed*. **2020**, *59*, 11020−11027.

(22) Kawashima, T.; Matsumoto, Y.; Sato, T.; Yamada, Y. M. A.; Kono, C.; Tsurusaki, A.; Kamikawa, K. Synthesis, Structure, and Complexation of an S-Shaped Double Azahelicene with Inner-Edge Nitrogen Atoms. *Chem. - Eur. J*. **2020**, *26*, 13170−13176.

(23) Zhang, L.; Song, I., Ahn, J.; Han, M.; Linares, M.; Surin, M.; Zhang, H.-J.; Oh, J. H.; Lin, J. π-Extended perylene diimide double-heterohelicenes as ambipolar organic semiconductors for broadband circularly polarized light detection. *Nat Commun*. **2021**, *12*, 142.

(24) Nogami, N.; Nagashima, Y.; Miyamoto, K.; Muranaka, A.; Uchiyama, M.; Tanaka, K. Asymmetric synthesis, structures, and chiroptical properties of helical cycloparaphenylenes. *Chem. Sci*. **2021**, *12*, 7858–7865.

(25) Bunz, U. H. F. The Larger *N*-Heteroacenes. *Pure Appl. Chem*. **2010**, *82*, 953–968.

(26) Bunz, U. H. F.; Freudenberg, J. *N*-Heteroacenes and *N*-Heteroarenes as *N*-Nanocarbon Segments. *Acc. Chem. Res*. **2019**, *52*, 1575–1587.

(27) Gangadhar, P. S.; Reddy, G.; Prasanntkumar, S.; Giribabu. L. Phenothiazine Functional Materials for Organic Optoelectronic Applications. *Phys. Chem. Chem. Phys*. **2021**, *23*, 14969−14996.

(28) Tanaka, K.; Sakamaki, D.; Fujiwara, H. Synthesis and Electronic Properties of

Directly Linked Dihydrodiazatetracene Dimers. *Chem. - Eur. J*. **2021**, *27*, 4430−4438.

(29) VanAllan, J. A.; Reynolds, G. A.; Maier, D. P. The Reaction of 12H-Benzo[*a*]phenothiazine and 12H-Benzo[*b*]phenoxazine with Certain Heterocyclic Azides *J. Org. Chem*. **1969**, *34*, 1691−1694.

(30) Inoue, Y.; Sakamaki, D.; Tsutsui, Y.; Gon, M.; Chujo, Y.; Seki, S. Hash-Mark-Shaped Azaacene Tetramers with Axial Chirality. *J. Am. Chem. Soc*. **2018**, *140*, 7152−7158.

(31) Wan, A.; Hwang, J.; Amy, F.; Kahn, A. Impact of electrode contamination on the α-NPD/Au hole injection barrier. *Org. Electron.* **2005**, 81, 2887.

(32) Fujikawa, T.; Mitoma, N.; Wakamiya, A.; Saeki, A.; Segawa, Y.; Itami, K. Synthesis, properties, and crystal structures of pi-extended double [6]helicenes: contorted multi-dimensional stacking lattice. *Org. Biomol. Chem.* **2017**, 15, 4697–4703.

(33) Haketa, Y.; Bando, Y.;Takaishi, K.; Uchiyama, M.; Muranaka, A.; Naito, M.; Shibaguchi, H.; Kawai, T.; Maeda, H. *Angew. Chem., Int. Ed*. **2012**, *51*, 7967−797.

(34) Morisaki, Y.; Gon, M.; Sasamori, T.; Tokitoh, N.; Chujo, Y. Planar Chiral Tetrasubstituted [2.2]Paracyclophane: Optical Resolution and Functionalization. *J. Am. Chem. Soc*. **2014**, *136*, 3350–3353.

(35) Y.; Gon, M.; Morisaki, Y.; Chujo, Y. Optically Active Cyclic Compounds Based on Planar Chiral [2.2]Paracyclophane: Extension of the Conjugated Systems and Chiroptical

Properties. *J. Mater. Chem. C* **2015**, *3*, 521–529.

(36) Morcillo, S. P.; Miguel, D.; Álvarez de Cienfuegos, L.; Justicia, J.; Abbate, S.; Castiglioni, E.; Bour, C.; Ribagorda, M.; Cárdenas, D. J.; Paredes, J. M.; Crovetto, L.; Choquesillo-Lazarte, D.; Mota, A. J.; Carreño, M. C.; Longhi, G.; Cuerva, J. M. Stapled Helical *o*-OPE Foldamers as New Circularly Polarized Luminescence Emitters based on Carbophilic Interactions with Ag(I)-sensitivity. *Chem. Sci*. **2016**, *7*, 5663– 5670.

(37) Sato, S.; Yoshii, A.; Takahashi, S.; Furumi, S.; Takeuchi, M.; Isobe, H. Chiral Intertwined Spirals and Magnetic Transition Dipole Moments Dictated by Cylinder Helicity. *Proc. Natl. Acad. Sci. U. S. A*. **2017**, *114*, 13097−13101.

(38) Kubo, H.; Shimizu, D.; Hirose, T.; Matsuda, K. Circularly Polarized Luminescence Designed from Molecular Orbitals: A Figure-Eight-Shaped [5]Helicene Dimer with D_2 Symmetry. *Org. Lett*. **2020**, *22*, 9276−9281.

(39) Kubo, H.; Hirose, T.; Nakashima, T.; Kawai, T.; Hasegawa, J.; Matsuda, K. Circularly Polarized Luminescence Designed from Molecular Orbitals: A Figure-Eight-Shaped [5]Helicene Dimer with D_2 Symmetry. *J. Phys. Chem. Lett.* **2021**, *12*, 686−695.

(40) Schellman, J. A. Circular Dichroism and Optical Rotation. *Chem. Rev*. **1975**, *75*, 323−331.

(41) Sprafke, J. K.; Kondratuk, D. V.; Wykes, M.; Thompson, A.L.; Hoffmann, M.;

Drevinskas, R.; Chen, W.-H.; Yong, C. K.; Kärnbratt, J.; Bullock, J. E.; Malfois, M.; Wasielewski, M. R.; Albinsson, B.; Herz, L. M.; Zigmantas, D.; Beljonne, D.; Anderson, H. L. Belt-Shaped π-Systems: Relating Geometry to Electronic Structure in a Six-Porphyrin Nanoring. *J. Am. Chem. Soc*. **2011**, *133*,17262−17273.

(42) Camacho, C.; Niehaus, T. A.; Itami, K.; Irle, S. Origin of the Size-Dependent Fluorescence Blueshift in [*n*]Cycloparaphenylenes. *Chem. Sci*. **2013**, *4*, 187−195.

(43) Wada, Y.; Shizu, K.; Kaji, H. Molecular Vibration Accelerates Charge Transfer Emission in a Highly Twisted Blue Thermally Activated Delayed Fluorescence Material. *J. Phys. Chem. A* **2021**, *125*, 21, 4534–4539.

(44) During the preparation of this manuscript, Isobe et al. reported that the dissymmetry factor is sensitive to subtle structural fluctuations in a cylinder-shaped chiral π-system: Fukunaga, T. M.; Sawabe, C.; Matsuno, T.; Takeya, J.; Okamoto, T.; Isobe, H. Manipulations of Chiroptical Properties in Belt-Persistent Cycloarylenes via Desymmetrization with Heteroatom Doping, *Angew. Chem., Int. Ed*. doi.org/10.1002/anie.202106992.

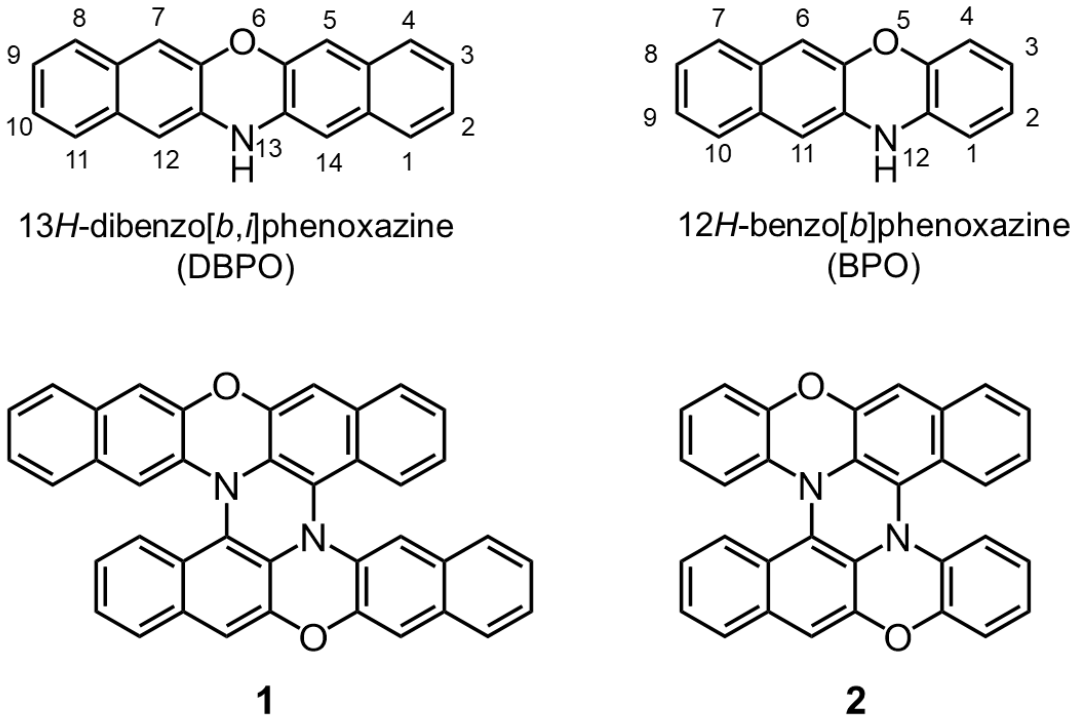

Figure 1. Structures of double heterohelicenes **1**, **2** and their monomers.

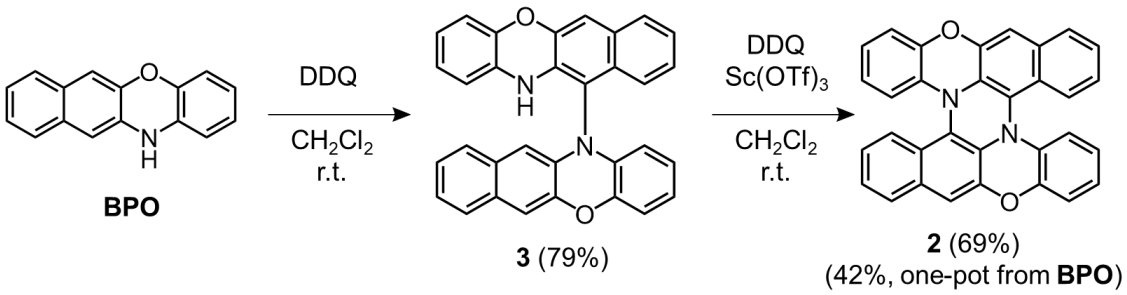

Scheme 1. Synthesis of **2**.

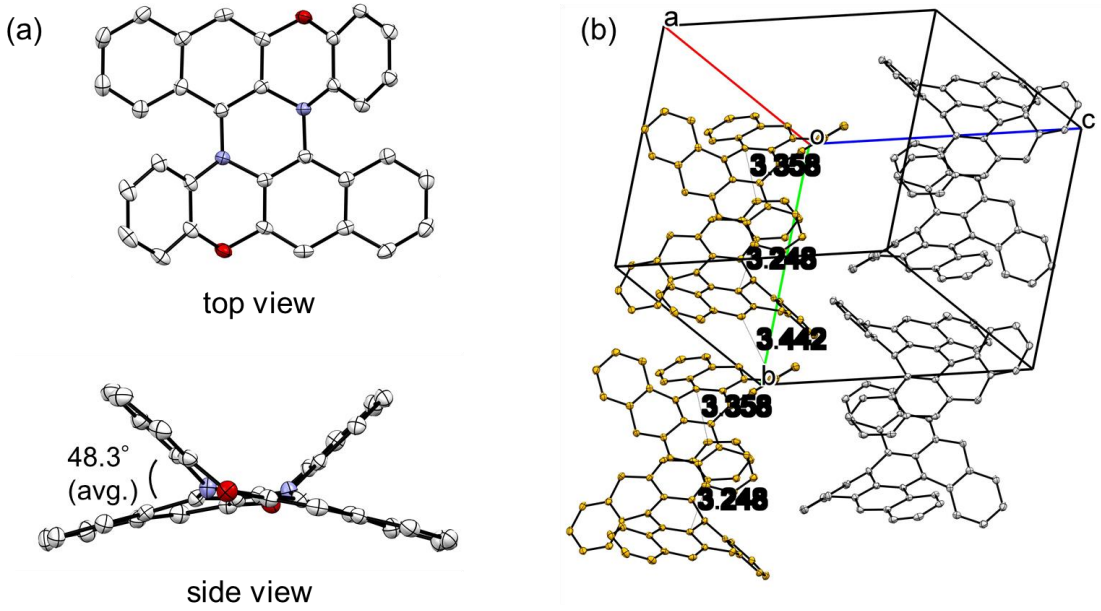

Figure 2. (a) ORTEP drawing of (*M*,*M*)-**2** in the racemic crystal and (b) crystal packing structure of racemic-**2**. Hydrogen atoms are omitted for clarity. Thermal ellipsoids are set at 50% probability. White and yellow in (b) represent the (*P*,*P*) and (*M*,*M*) isomers, respectively.

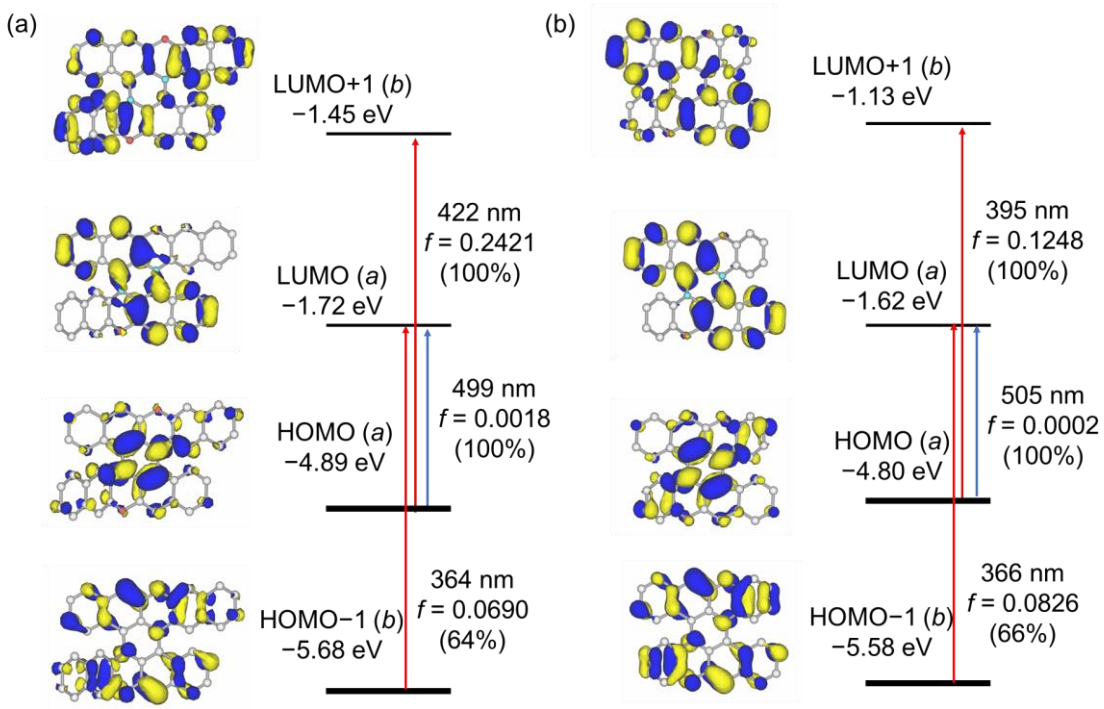

Figure 3. Frontier Kohn-Sham molecular orbitals of **1** and **2** and TD-DFT calculated electronic transitions calculated at the B3LYP-GD3BJ/6-311G(2d,p) level.

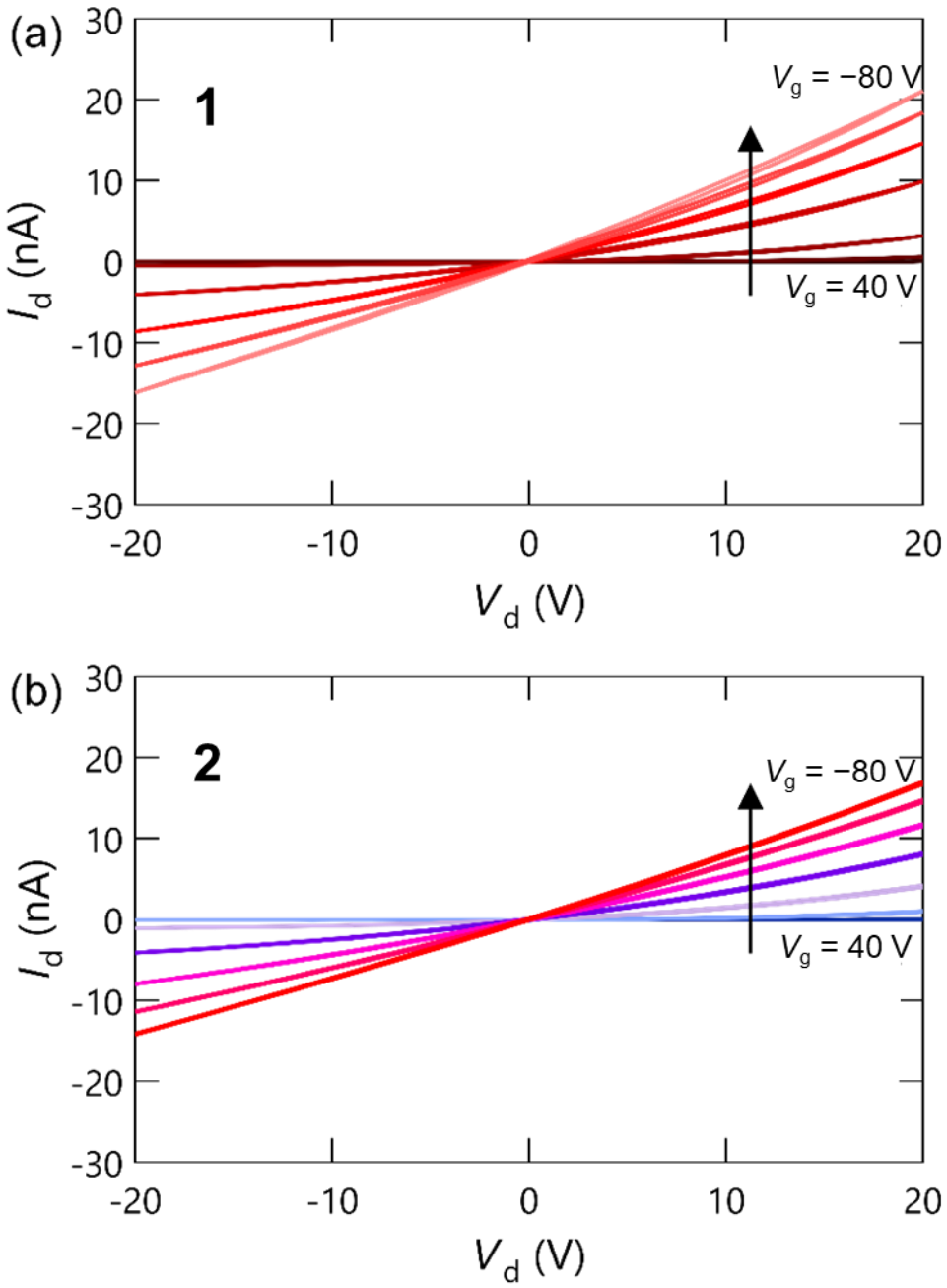

Figure 4. The drain voltage (V_d) dependences of drain currents (I_d) obtained at gate voltages (V_g) between 40 V and −80 V at intervals of 20 V for (a) **1** and (b) **2**.

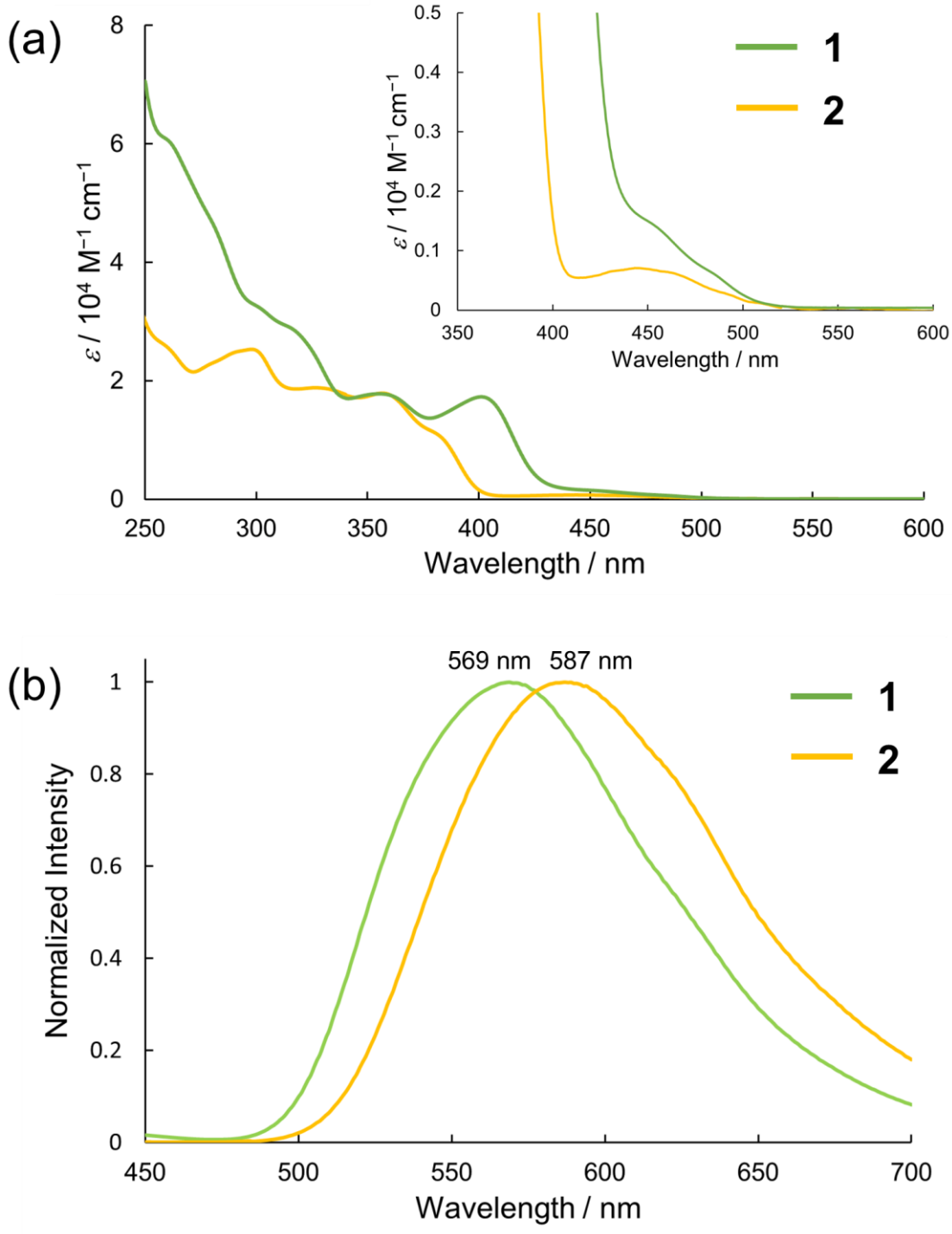

Figure 5. (a) Absorption and (b) emission spectra (λ_{ex} = 365 nm) of racemic-**1** and **2** in dichloromethane at room temperature.

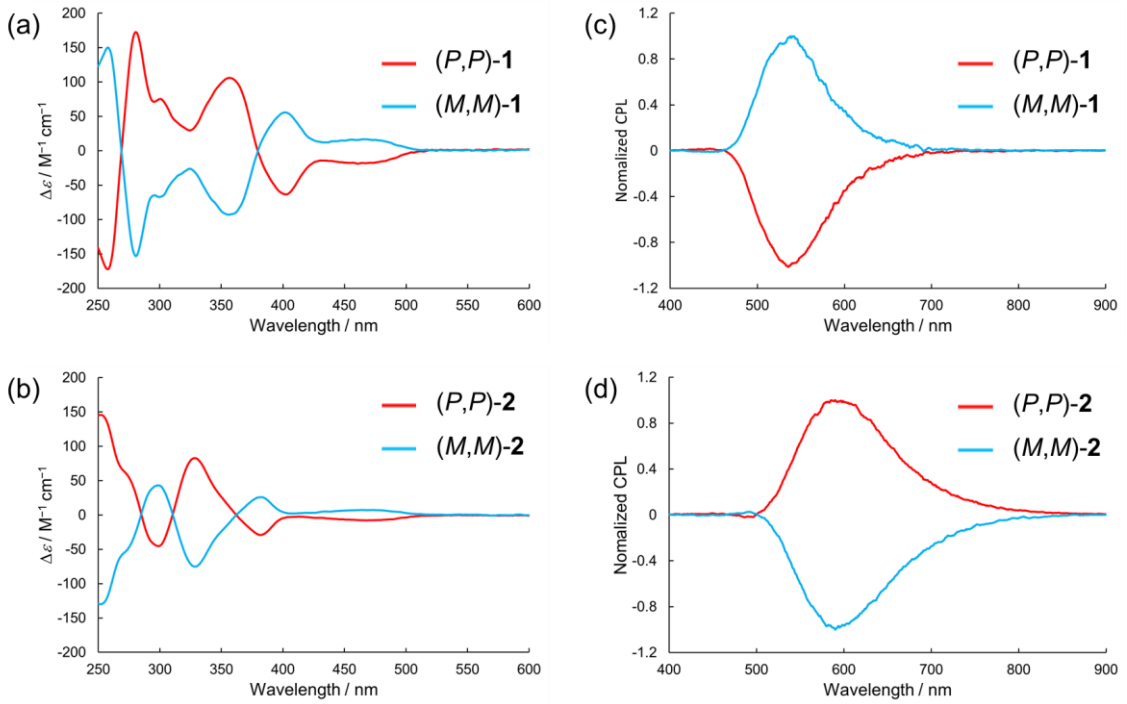

Figure 6. CD spectra of (a) **1** and (b) **2** (1×10^{-5} M in dichloromethane) and CPL spectra of (c) **1** and (d) **2** (2×10^{-4} M in dichloromethane, $\lambda_{ex} = 300$ nm) at room temperature.

Table 1. Photophysical properties of **1** and **2** in dichloromethane.

Compound	$\lambda_{max,\,em}$ / nm	Φ_f	τ_f / ns	k_f / s^{-1}	k_{nr} / s^{-1} [a]	g_{CD} [b]	g_{CPL} [b]
1	569	0.038	13.4	2.8×10^6	7.2×10^7	$+1.7\times10^{-2}$ (470 nm)	$+2.3\times10^{-2}$ (490 nm)
2	587	0.035	21.1	1.7×10^6	4.6×10^7	$+1.3\times10^{-2}$ (470 nm)	-1.3×10^{-2} (590 nm)

[a] k_{nr}: nonradiative decay rate constant, $k_{nr} = (1 - \Phi_f) / \langle\tau_f\rangle$. [b] (*M*,*M*)-isomer

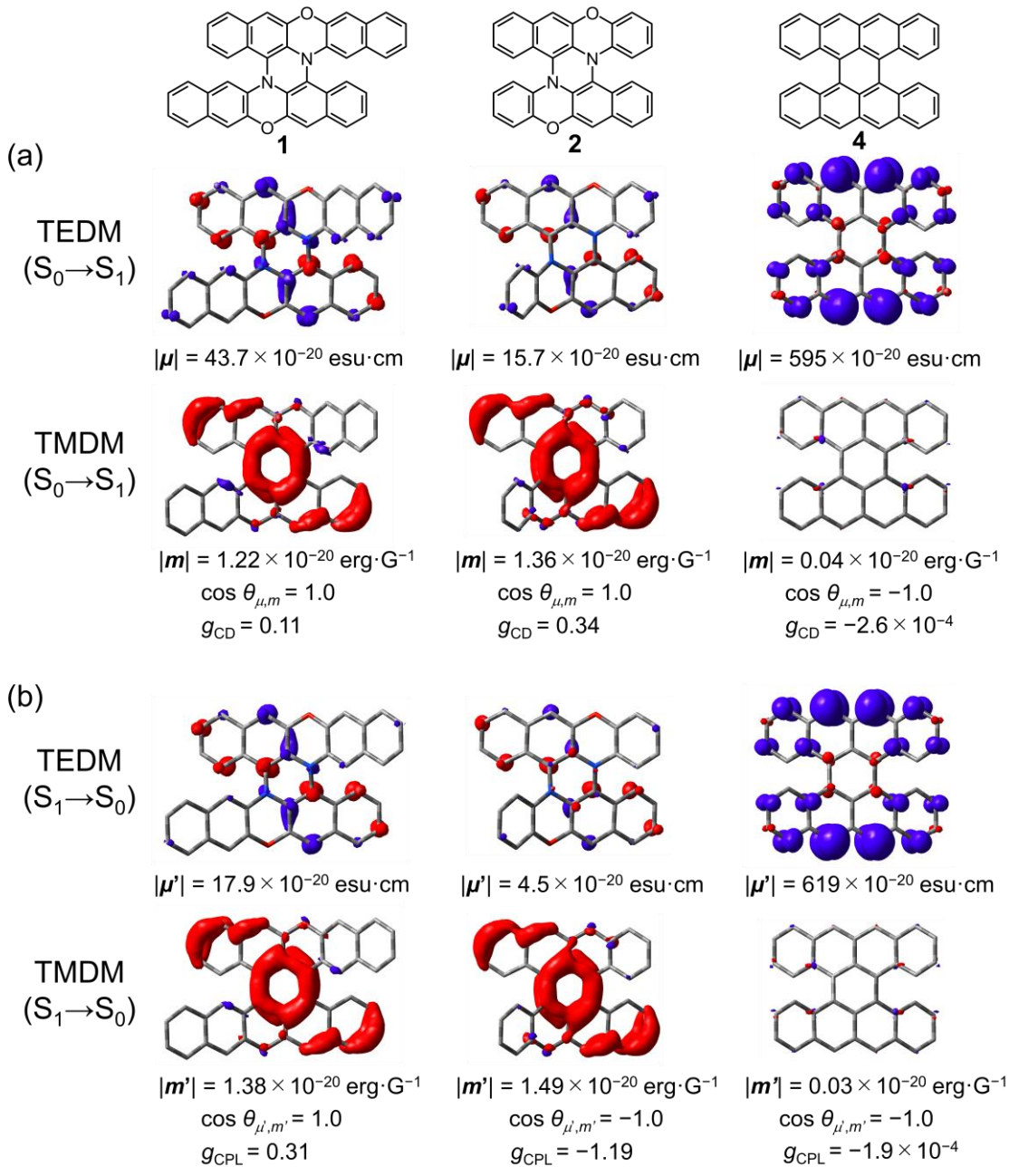

Figure 7. Results of TEDM and TMDM analysis of (*M*,*M*)-**1**, **2**, and **4** for (a) $S_0 \rightarrow S_1$ transitions and for (b) $S_1 \rightarrow S_0$ transitions. TD-DFT calculations were performed at the B3LYP-GD3BJ/6-311G(2d,p) level. Isosurface values were set at 0.004 for TEDM densities and 0.002 for TMDM densities, respectively.

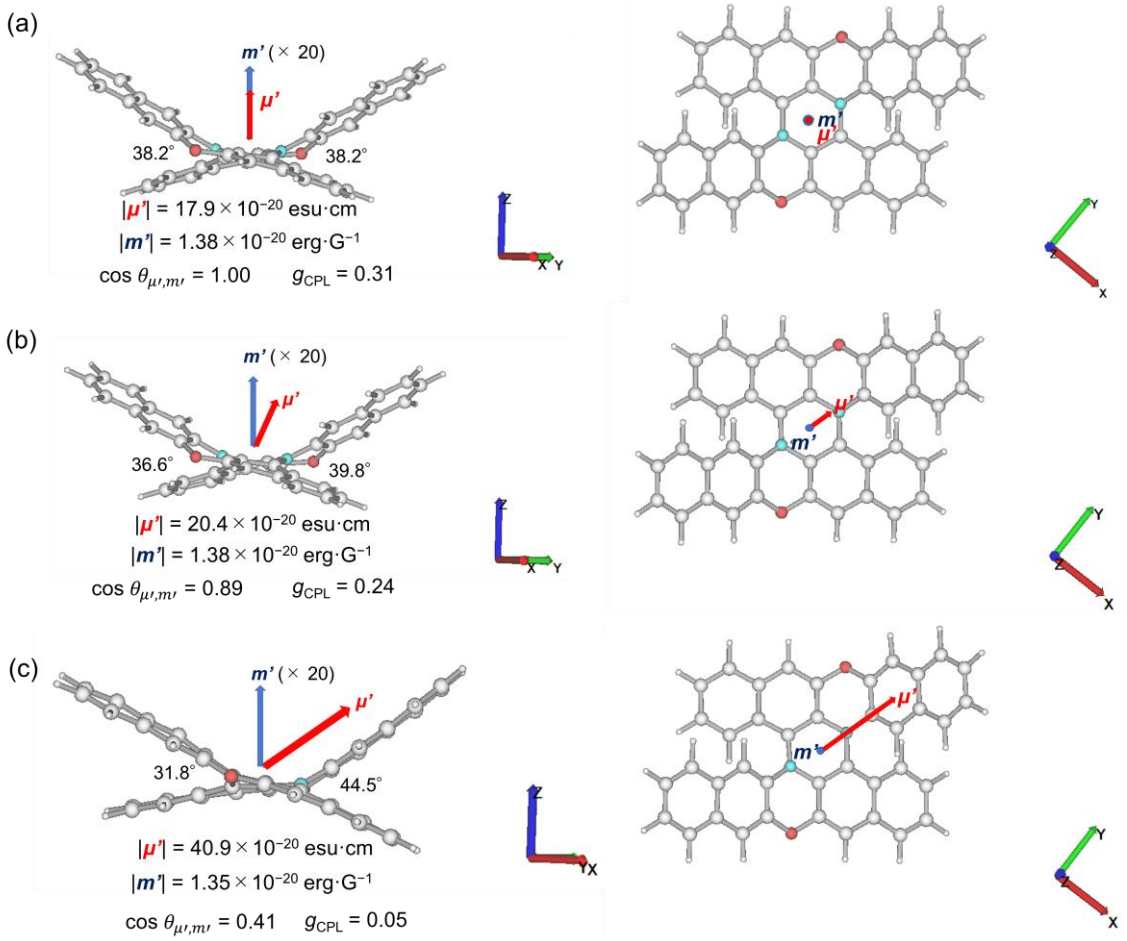

Figure 8. Changes of the TEDM, TMDM, and g_{CPL} of (*M*,*M*)-**1** in the S_1 state upon deformation along mode 3 calculated at the B3LYP-GD3BJ/6-311G(2d,p) level. (a) λ = 0, (b) λ = 0.5, and (c) λ = 2 (for the definition of the deformation parameter λ, see page 30 of SI).

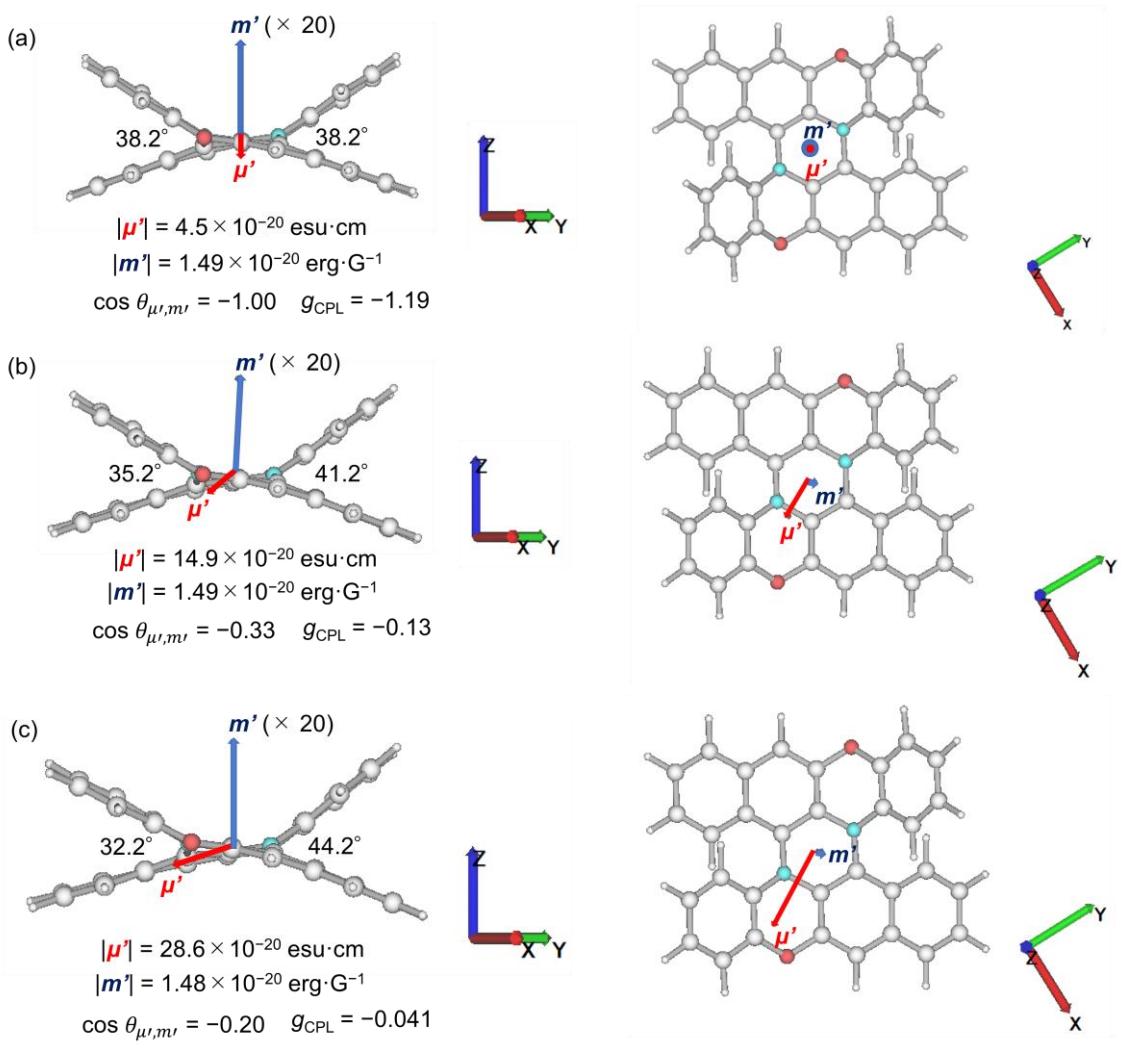

Figure 9. Changes of the TEDM, TMDM, and g_{CPL} of (*M*,*M*)-**2** in the S_1 state upon deformation along mode 4 calculated at the B3LYP-GD3BJ/6-311G(2d,p) level. (a) λ = 0, (b) λ = 0.5, and (c) λ = 1.